This is the accepted manuscript made available via CHORUS. The article has been published as:

Iodine interstitials as a cause of nonradiative recombination in hybrid perovskites

Xie Zhang, Mark E. Turiansky, Jimmy-Xuan Shen, and Chris G. Van de Walle

Phys. Rev. B **101**, 140101 — Published 15 April 2020

DOI: 10.1103/PhysRevB.101.140101

Iodine interstitials as a cause of nonradiative recombination in hybrid perovskites

Xie Zhang[1],[*] Mark E. Turiansky[2], Jimmy-Xuan Shen[2], and Chris G. Van de Walle[1][†]
[1] *Materials Department, University of California, Santa Barbara, CA 93106-5050, USA and*
[2] *Department of Physics, University of California, Santa Barbara, CA 93106-9530, USA*

The identification of deep-level defects that act as detrimental nonradiative recombination centers is critical for optimizing the optoelectronic performance of hybrid perovskites. Although extensive studies have been devoted to revealing the nature of deep-level defects in hybrid perovskites, it is still unclear what defects are responsible for the experimentally observed nonradiative recombination rates. Employing first-principles approaches, we quantitatively show that the iodine interstitial is a dominant nonradiative recombination center in methylammonium-lead iodide. This important insight points to a target for defect engineering in order to further improve the performance of hybrid perovskites.

As excellent optoelectronic materials with solar conversion efficiencies greater than 25%[1], hybrid perovskites have received enormous attention. Defect-assisted nonradiative carrier recombination is one of the key processes that cause energy dissipation, limiting the efficiency. Identifying the critical defects and quantifying their induced nonradiative recombination rates are crucial for optimizing devices performance[2]. Research efforts have thus turned toward the identification of deep-level defects in hybrid perovskites from both theory[3–6] and experiment[7–9] to further improve the solar-cell efficiencies.

Early first-principles studies of the native point defects in hybrid perovskites[3,4] claimed that the energetically favorable defects are not efficient nonradiative recombination centers due to the lack of mid-gap states. However, this result conflicts with experimental reports[7–9] clearly showing the presence of deep-level defects in hybrid perovskites, as well as measurement of nonradiative recombination coefficients on the order of 10^7 s^{-1}[10–14].

The discrepancy has been attributed[5,6] to the use of semilocal exchange-correlation functionals and the neglect of spin-orbit coupling (SOC) in the early theoretical works[3,4]. With a more accurate approach, several deep-level defects were identified in the prototypical hybrid perovskite $\mathrm{MAPbI_3}$ ($\mathrm{MA{=}CH_3NH_3}$), namely, the iodine interstitial (I_i), the Pb vacancy (V_{Pb}), and iodine substituting on an MA site ($\mathrm{I_{MA}}$). It is still an open question whether these defects are efficient nonradiative recombination centers and actually responsible for the nonradiative recombination rates observed in experiments.

In the present work we show, by explicitly computing the defect-assisted nonradiative recombination coefficients from first principles, that the iodine interstitial has a total nonradiative capture coefficient on the order of 10^{-8} cm^{3}s^{-1} at room temperature and is the likely cause of the experimentally measured nonradiative recombination rates in $\mathrm{MAPbI_3}$. Such insight into the dominant defect is critical for understanding the mechanisms of the performance of hybrid perovskites and further improvement of materials design via defect engineering.

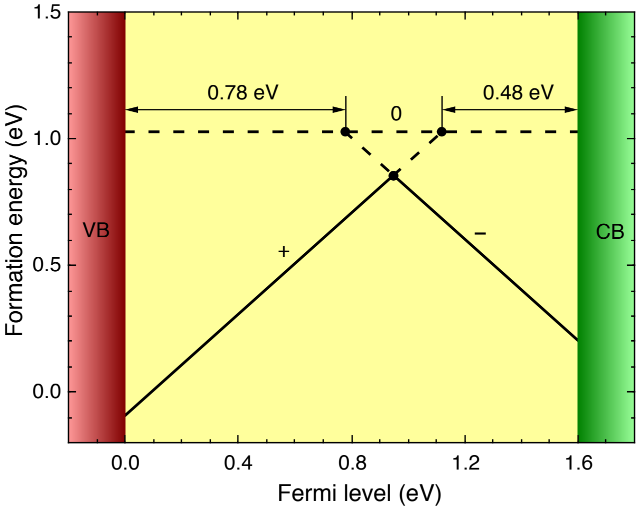

FIG. 1. Formation energy of the iodine interstitial, I_i, as a function of the Fermi level under I-rich conditions. The (0/−) charge-state transition occurs at 0.78 eV above the valence-band maximum (VBM), and the (+/0) transition at 0.48 eV below the conduction-band minimum (CBM).

We first focus on I_i and will discuss the behavior of V_{Pb} and $\mathrm{I_{MA}}$ later. Figure 1 shows the formation energy of I_i in three charge states (−, 0, and +) in $\mathrm{MAPbI_3}$ under I-rich conditions, computed using density functional theory with the Heyd-Scuseria-Ernzerhof (HSE)[15] hybrid functional and including SOC (see more details in the Supplemental Material[16]). The formation energies of I_i^+ or I_i^- intersect at 0.95 eV above the valence-band maximum (VBM), and I_i^0 is energetically less favorable than either I_i^+ or I_i^- over the entire range of Fermi levels in the band gap; this is characteristic of so-called negative-U behavior. The (+/−) transition level, however, does not govern nonradiative recombination, since a defect cannot capture two electrons (or holes) at once[17]. The relevant charge-state transitions are (0/−) and (+/0), which are located at 0.78 eV above the VBM and 0.48 eV below the conduction-band minimum (CBM). The (+/0) transition level is very close to the value (0.57 eV below the CBM) reported in Ref. 6, while the (−/0) transition level is somewhat farther from the VBM than in Ref. 6 (0.29 eV). We attribute the difference to three causes. First, in our calculations we relax the defect configurations using the accurate HSE+SOC scheme, while in Ref. 6 structural relaxations were performed using a semilocal Perdew-Burke-Ernzerhof (PBE)[18] functional without SOC. Second, as discussed in more detail below, we identified a different stable configuration for I_i^0. Third, the orthorhombic perovskite structure is used for our defect calculations, while the tetragonal perovskite structure was adopted in Ref. 6. A detailed comparison of the defect configurations obtained by HSE+SOC and PBE relaxations is provided in Supplemental Material[16].

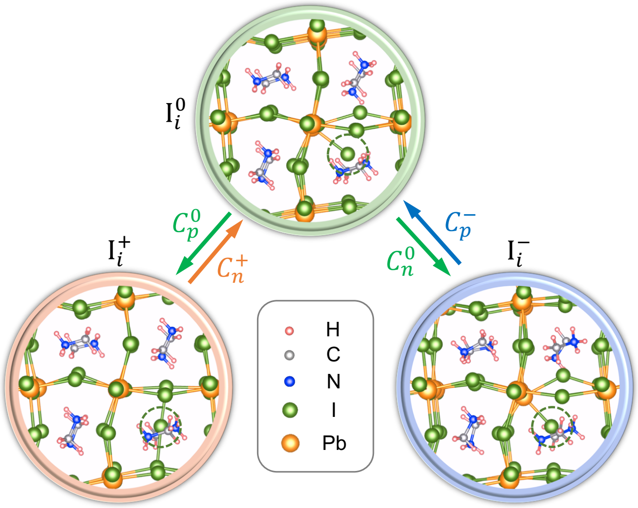

FIG. 2. Local atomic structures of I_i in three charge states (+, 0, and −). The arrows and labels show the relevant carrier capture processes. In the labels of capture coefficients, the subscript denotes the carrier being captured (n for electrons and p for holes) while the superscript denotes the charge state of the initial configuration. The green dashed circles highlight the location of the I interstitials.

Figure 2 shows the local atomic structures of I_i in the three charge states discussed above. For I_i^+ the interstitial I atom sits midway between two I atoms that are second-nearest neighbors, forming an I-trimer. By capturing an electron (C_n^+), I_i^+ transforms to I_i^0, in which the interstitial I atom bonds with a neighboring Pb atom and pushes a neighboring I atom away toward an adjacent interstitial position. With another electron being captured (C_n^0), the two I atoms (the I_i and a lattice I atom) separate further apart, forming I_i^-. Similarly, there exist two hole-capture processes through the $\mathrm{I}_i^- \to \mathrm{I}_i^0 \to \mathrm{I}_i^+$ transition, and the corresponding capture coefficients (C_p^- and C_p^0) are labeled in Fig. 2. By balancing electron and hole capture under steady-state conditions[19], the total capture coefficient (C_{tot}) can be derived as

$$C_{\mathrm{tot}} = \frac{C_n^0 + C_p^0}{1 + \frac{C_n^0}{C_p^-} + \frac{C_p^0}{C_n^+}} \tag{1}$$

To determine the total capture coefficient we calculate the above-mentioned four capture coefficients (see the Supplemental Material[16] for details). Figure 3 shows the calculated configuration coordinate diagrams for the $\mathrm{I}_i^+ \leftrightarrow \mathrm{I}_i^0$ and $\mathrm{I}_i^0 \leftrightarrow \mathrm{I}_i^-$ transitions. These diagrams map the potential energy surfaces of the charge-state transitions as a function of a generalized configuration coordinate (Q)[20]. Q is computed using the definition in Ref. 2. Figure 3a characterizes two capture processes. Starting from I_i^+ with an electron (e^-) at the CBM and a hole (h^+) at the VBM, I_i^+ captures the electron and transitions to I_i^0. In a semi-classical picture, the process needs to overcome an energy barrier (ΔE_n^+) as determined by the intersection between the potential energy surfaces (the green and orange curves in Fig. 3a). Similarly, the hole can be captured by I_i^0 and the system relaxes back to I_i^+ (the blue curve in Fig. 3a). For this hole capture process the energy barrier is almost zero, which indicates that this process is very fast. The small barrier results from strong anharmonicity in the potential energy surface of I_i^+; the pronounced impact of anharmonicity on the barrier is enabled by the large structural difference ($\Delta Q \approx 15.0\ \mathrm{amu}^{1/2}$Å) between I_i^+ and I_i^0.

A similar analysis can be performed for the (0/−) charge-state transition as shown in Fig. 3b. The ΔQ is even greater and the potential energy surface of I_i^0 exhibits a metastable minimum at the equilibrium configuration of I_i^-. This metastable configuration is actually the one reported for I_i^0 in Ref. 6. As shown in Fig. 3b, this metastable configuration is energetically less favorable than the one presented in Fig. 2 for the neutral charge state by 0.69 eV. The energy barriers of the (0/−) charge-state transition (ΔE_n^0 and ΔE_p^-) are both moderate, which indicates reasonably fast electron and hole capture.

The above analysis of the configuration coordinate diagrams provides a qualitative understanding of the capture processes within a semi-classical picture. The exact capture coefficients are determined by the quantum-mechanical vibronic overlap between each two potential energy surfaces and the strength of electron-phonon coupling[2]. We show the explicitly calculated capture coefficients in Fig. 4a. As expected from its negligible energy barrier, the hole capture by I_i^0 (C_p^0) has a high coefficient, on the order of $10^{-5}\ \mathrm{cm}^3\mathrm{s}^{-1}$. Even though the energy barrier (ΔE_p^-) for the hole capture by I_i^- (C_p^-) seems to be higher than the ones for the other cases, the potential energy surfaces of I_i^- and I_i^0 (the orange and blue curves in Fig. 3b) are very close when $Q < 0$, which enables a strong overlap of the vibronic wavefunctions. Indeed, the hole capture coefficient of I_i^- (C_p^-) is $3.5 \times 10^{-8}\ \mathrm{cm}^3\mathrm{s}^{-1}$ at room temperature, even higher than the electron capture coefficient of I_i^+ (C_n^+). This illustrates the importance of explicitly calculating the capture coefficients, and not just relying on the semi-classical barriers ΔE. Throughout the entire temperature range shown, electron capture by I_i^+ (C_n^+) is the slowest with a coefficient of $0.7 \times 10^{-8}\ \mathrm{cm}^3\mathrm{s}^{-1}$ at room temperature, limiting the total capture coefficient (the black dashed

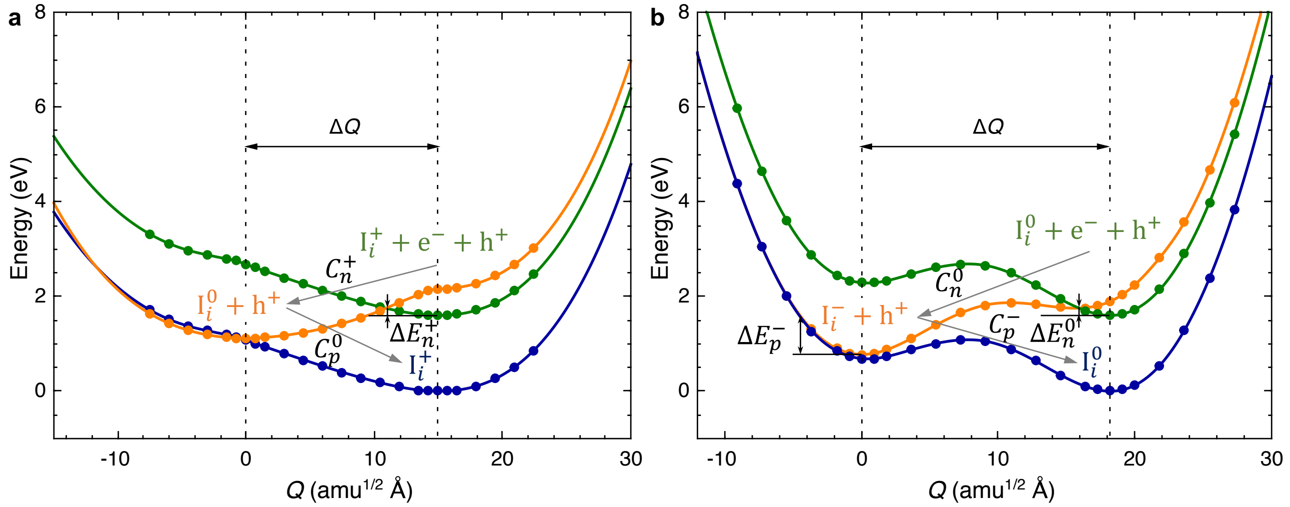

FIG. 3. (a) Configuration coordinate diagram for (a) the (+/0) and (b) the (0/−) charge-state transitions of the iodine interstitial.

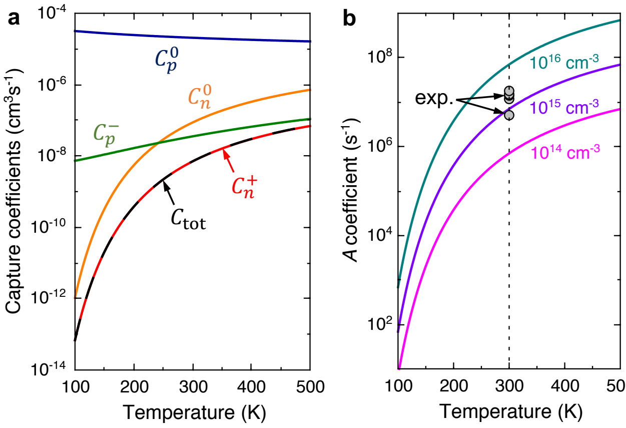

FIG. 4. (a) Nonradiative capture coefficients of I_i as a function of temperature. (b) Nonradiative recombination coefficient A of I_i as a function of temperature for three different defect densities (10^{14}, 10^{15}, and 10^{16} cm^{-3}). The black circles in (b) correspond to the experimental A coefficients reported in the literature[10–14].

line in Fig. 4a).

Looking back at the formation-energy diagram in Fig. 1, we conclude that the conventional criterion for judging the capture coefficient based on the position of the charge-state transition level does not apply here. This criterion assumes that the electron and hole capture coefficients decline roughly exponentially with the transition energy (the energy difference between the transition level and the band edge from which a carrier is captured)[21]. Based on Fig. 1, hole capture by I_i^0 (described by coefficient C_p^0) is thus expected to be rate-limiting. The (0/+) transition level is 1.12 eV away from the VBM, the furthest from the band edge among the four capture processes. Conventional wisdom would then indicate that hole capture by I_i^0 should be the slowest among the four processes. The calculations show that, in fact, it is the fastest. Similarly, electron capture by I_i^+ (C_n^+) should, in principle, be the fastest [based on the (+/0) level being only 0.48 eV away from the CBM], but it turns out to be the rate-limiting step of the overall capture process. This anomalous behavior stems primarily from strong anharmonicity, and leads to the relatively fast nonradiative recombination induced by I_i. We note that the strong anharmonicity is an intrinsic feature of the Pb-I inorganic lattice, which is present in the all-inorganic halide perovskite $\mathrm{CsPbI_3}$ as well[22].

We now discuss the impact of V_{Pb} and $\mathrm{I_{MA}}$ on nonradiative recombination. V_{Pb} has a deep charge-state transition level in the band gap, but as shown in Ref. 6, this level corresponds to a (0/2−) transition. The relevant transitions are (0/−) and (−/2−), and four capture processes (two for electron capture and two for hole capture) are associated with these two transitions. The overall capture coefficient is limited by the slowest process; based on the conventional criterion, this should be electron capture by V_{Pb}^-, since the (−/2−) transition level is far from the CBM. Still, as we have shown for I_i, anharmonicity may change the capture barriers and coefficients. Hence, we have performed explicit calculations, which show that V_{Pb} indeed causes negligible nonradiative recombination. Similarly, we can rule out $\mathrm{I_{MA}}$ as an efficient nonradiative center; again, this defect has a (0/2−) transition level deep in the band gap, but it will not cause strong nonradiative recombination due to slow electron capture by $\mathrm{I_{MA}^-}$. In addition, $\mathrm{I_{MA}}$ has a high formation energy (much higher than I_i and V_{Pb}), which means that its concentration will be very low.

With the total capture coefficient determined, we can now compute the nonradiative recombination coefficient A, which is defined as $A = N_{\mathrm{def}} C_{\mathrm{tot}}$, where N_{def} is the defect density. We cannot determine the defect density from theory, since it depends on the growth and processing conditions. An estimate can be made based on experiment; for instance, Ref. 9 reported a defect density on the order of 10^{15} cm^{-3}. In Fig. 4b we plot the A coefficient as a function of temperature for three reasonable defect densities (10^{14}, 10^{15}, and 10^{16} cm^{-3}) and compare it with experimentally reported A coefficients at room temperature[10–14]. The experimental A values cluster around 10^7 s^{-1}, with a spread of less than one order of magnitude. The theoretically computed A coefficient at a defect density of 10^{15} cm^{-3} agrees well with the experimental values at room temperature. This good agreement indicates that the iodine interstitial is likely responsible for the observed defect-assisted nonradiative recombination in $\mathrm{MAPbI_3}$. Overall, the recombination coefficient is still moderate, yielding a recombination lifetime on the order of 0.1 μs, which is comparable to those in GaN ($0.1-1.0$ μs[23]) and GaAs ($0.25-2.0$ μs[24]). The relatively slow nonradiative recombination is one of the major reasons why the carrier lifetime in hybrid perovskites is long.

In conclusion, we have systematically studied the nonradiative recombination induced by native point defects in $\mathrm{MAPbI_3}$ using first-principles approaches. Our accurately computed nonradiative capture coefficients demonstrate that electron capture by I_i^+ is the rate-limiting step, leading to a capture coefficient of 0.7×10^8 cm^{3}s^{-1}. The iodine interstitial is likely responsible for the experimentally observed nonradiative recombination rates. This study demonstrates the possibility of enhancing the optoelectronic performance of hybrid perovskites by controlling incorporation of iodine interstitial defects. For this purpose, I-poor synthesis conditions are, in principle, favored. Such synthesis conditions may trigger the formation of iodine vacancies (V_I). V_I does not have any levels in the band gap, and therefore cannot act as an efficient recombination center, but it may degrade the performance of hybrid perovskites in other ways.

This work was supported by the U.S. Department of Energy (DOE), Office of Science, Basic Energy Sciences (BES) under Award No. DE-SC0010689. Computational resources were provided by the Extreme Science and Engineering Discovery Environment (XSEDE), which is supported by National Science Foundation grant number ACI-1548562.

---

[*] xiezhang@ucsb.edu

[†] vandewalle@mrl.ucsb.edu

[1] "Best research-cell efficiency chart," `https://www.nrel.gov/pv/assets/pdfs/best-research-cell-efficiencies.20191106.pdf`, accessed: 2019-11-06.

[2] A. Alkauskas, Q. Yan, and C. G. Van de Walle, Phys. Rev. B **90**, 075202 (2014).

[3] W.-J. Yin, T. Shi, and Y. Yan, Appl. Phys. Lett. **104**, 063903 (2014).

[4] A. Buin, P. Pietsch, J. Xu, O. Voznyy, A. H. Ip, R. Comin, and E. H. Sargent, Nano Lett. **14**, 6281 (2014).

[5] M.-H. Du, J. Phys. Chem. Lett. **6**, 1461 (2015).

[6] D. Meggiolaro, S. G. Motti, E. Mosconi, A. J. Barker, J. Ball, C. Andrea Riccardo Perini, F. Deschler, A. Petrozza, and F. De Angelis, Energy Environ. Sci. **11**, 702 (2018).

[7] A. Baumann, S. Väth, P. Rieder, M. C. Heiber, K. Tvingstedt, and V. Dyakonov, J. Phys. Chem. Lett. **6**, 2350 (2015).

[8] S. Heo, G. Seo, Y. Lee, D. Lee, M. Seol, J. Lee, J.-B. Park, K. Kim, D.-J. Yun, Y. S. Kim, J. K. Shin, T. K. Ahn, and M. K. Nazeeruddin, Energy Environ. Sci. **10**, 1128 (2017).

[9] W. S. Yang, B.-W. Park, E. H. Jung, N. J. Jeon, Y. C. Kim, D. U. Lee, S. S. Shin, J. Seo, E. K. Kim, J. H. Noh, and S. I. Seok, Science **356**, 1376 (2017).

[10] Y. Yamada, T. Nakamura, M. Endo, A. Wakamiya, and Y. Kanemitsu, J. Am. Chem. Soc. **136**, 11610 (2014).

[11] R. L. Milot, G. E. Eperon, H. J. Snaith, M. B. Johnston, and L. M. Herz, Adv. Funct. Mater. **25**, 6218 (2015).

[12] D. Bi, W. Tress, M. I. Dar, P. Gao, J. Luo, C. Renevier, K. Schenk, A. Abate, F. Giordano, J.-P. Correa Baena, J.-D. Decoppet, S. M. Zakeeruddin, M. K. Nazeeruddin, M. Grätzel, and A. Hagfeldt, Sci. Adv. **2**, e1501170 (2016).

[13] J. M. Richter, M. Abdi-Jalebi, A. Sadhanala, M. Tabachnyk, J. P. Rivett, L. M. Pazos-Outón, K. C. Gödel, M. Price, F. Deschler, and R. H. Friend, Nat. Commun. **7**, 13941 (2016).

[14] H. Zhu, M. T. Trinh, J. Wang, Y. Fu, P. P. Joshi, K. Miyata, S. Jin, and X. Y. Zhu, Adv. Mater. **29**, 1603072 (2017).

[15] J. Heyd, G. E. Scuseria, and M. Ernzerhof, J. Chem. Phys. **118**, 8207 (2003).

[16] See Supplemental Material at [URL] for computational details and a structural comparison of the defect configurations relaxed using different schemes, which includes Refs.[25–30].

[17] N. Bagraev and V. Mashkov, Solid State Commun. **65**, 1111 (1988).

[18] J. P. Perdew, K. Burke, and M. Ernzerhof, Phys. Rev. Lett. **77**, 3865 (1996).

[19] A. Alkauskas, C. E. Dreyer, J. L. Lyons, and C. G. Van de Walle, Phys. Rev. B **93**, 201304(R) (2016).

[20] A. Alkauskas, M. D. McCluskey, and C. G. Van de Walle, J. Appl. Phys. **119**, 181101 (2016).

[21] C. H. Henry and D. V. Lang, Phys. Rev. B **15**, 989 (1977).

[22] X. Zhang, M. E. Turiansky, and C. G. Van de Walle, J. Phys. Chem. C (2020), 10.1021/acs.jpcc.0c01324.

[23] F. Olivier, A. Daami, C. Licitra, and F. Templier, Appl. Phys. Lett. **111**, 022104 (2017).

[24] E. Yablonovitch, R. Bhat, J. P. Harbison, and R. A. Logan, Appl. Phys. Lett. **50**, 1197 (1987).

[25] P. E. Blöchl, Phys. Rev. B **50**, 17953 (1994).

[26] G. Kresse and J. Furthmüller, Phys. Rev. B **54**, 11169 (1996).

[27] H. J. Monkhorst and J. D. Pack, Phys. Rev. B **13**, 5188 (1976).

[28] T. Baikie, Y. Fang, J. M. Kadro, M. Schreyer, F. Wei, S. G. Mhaisalkar, M. Grätzel, and T. J. White, J. Mater. Chem. A **1**, 5628 (2013).

[29] C. Freysoldt, B. Grabowski, T. Hickel, J. Neugebauer, G. Kresse, A. Janotti, and C. G. Van de Walle, Rev. Mod. Phys. **86**, 253 (2014).

[30] C. Freysoldt, J. Neugebauer, and C. G. Van de Walle, Phys. Rev. Lett. **102**, 016402 (2009).